Science Advances
AAAS

advances.sciencemag.org/cgi/content/full/7/2/eaba4261/DC1

Supplementary Materials for

3D printing of highly stretchable hydrogel with diverse UV curable polymers

Qi Ge*, Zhe Chen, Jianxiang Cheng, Biao Zhang*, Yuan-Fang Zhang, Honggeng Li, Xiangnan He, Chao Yuan, Ji Liu, Shlomo Magdassi, Shaoxing Qu*

*Corresponding author. Email: geq@sustech.edu.cn (Q.G.); iambzhang@nwpu.edu.cn (B.Z.); squ@zju.edu.cn (S.Q.)

Published 6 January 2021, *Sci. Adv.* **7**, eaba4261 (2021)
DOI: 10.1126/sciadv.aba4261

The PDF file includes:

Other Supplementary Material for this manuscript includes the following:

(available at advances.sciencemag.org/cgi/content/full/7/2/eaba4261/DC1)

Supplementary Materials

Note S1: We printed all the hydrogel-polymer heterogenous 3D structures on a self-built DLP based Multimaterial 3D printing system. We reported the details on the development of multimaterial 3D printer in a previously published article (*26*). Supplementary Fig. S1A presents the basic components of the apparatus where photocurable puddles are subjected to UV projections in the upward direction through a glass plate that is covered on the top surface with optically-clear PTFE silicone-adhesive tape. The plate is horizontally-translated using a translational stage (LTS150, Thorlabs Inc., Newton, NJ, USA). Various photocurable resins are contained in different syringes and deposited on the glass plate by automatically controlling the linear stages connected to the syringes, which avoids the direction contact between the printed structure and polymer resins in containers. Customized 405 nm-wavelength UV patterns are projected using a digital light processing (DLP) light engine (CEL5500, Digital Light Innovations, Austin, TX, USA) upward through the glass plate. The electronic components of the apparatus are controlled in sequence using codes written in LabVIEW 2016 (National Instruments, Austin, TX, USA).

Supplementary Fig. S1B depicts the primary steps used in the fabrication of hydrogel-polymer heterogenous structures. In STEP I, the translational stage delivers the polymer puddle below the printed structure, and a UV is irradiated to cure a new layer of polymer. In STEP II, the printing stage is left up, and the translational stage moves the material puddles away from the printing stage. The air jet is applied to blow away the residual polymer resin left on the printed structure. In STEP III, the translational stage delivers the hydrogel puddle below the printed structure, and a UV is irradiated to cure a new layer of hydrogel. As the same as The STEP II, in STEP IV, the air jet is applied to blow away the residual hydrogel solution left on the printed structure. The four steps repeat until the all whole heterogenous structure is printed. The material exchange process can also be seen in Movie S1.

The air jet assisted droplet delivery multimaterial DLP based 3D printing system can greatly reduce the material contamination during the material exchange process. The low

degree of the material contamination is demonstrated in Supplementary Fig. S1C where no obvious contamination is observed in a hydrogel puddle after printing. The current multimaterial 3D printing enables us to fabricate highly complex 3D structures with high resolution and sharp material transition between hydrogel and polymer. To demonstrate this, we printed a 3.8mm × 3.8 mm × 3.8 mm transparent hydrogel cube reinforced by an orange rigid Kelvin form (Supplementary Fig. S1D). A microscopic image in Supplementary Fig. S1E shows the sharp material transition between the transparent hydrogel and orange rigid polymer, and the diameter of the rigid Kelvin form is about 100 μm.

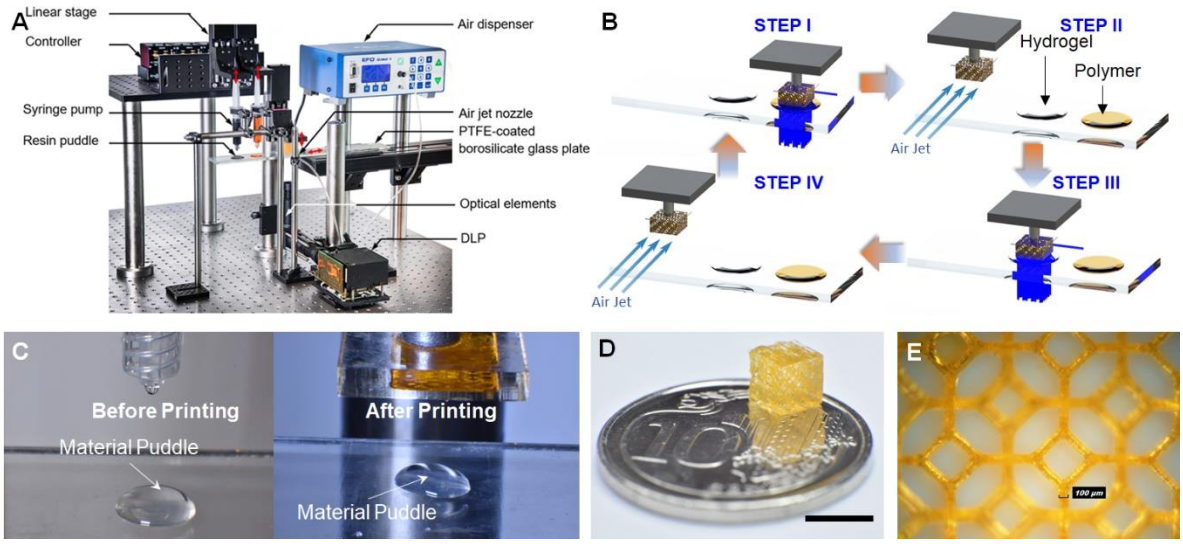

Fig. S1. The air jet assisted DLP based multimaterial 3D printing system. (**A**) A snapshot of the printing system. (**B**) Schematic illustrations of the air jet assisted material exchange process. (**C**) Photographs of transparent hydrogel puddle on the glass plate before and after printing. (**D**) A printed rigid Kelvin reinforced transparent hydrogel cube sitting on a 10 cent Singapore coin (scale bar: 5 mm). (**E**) A microscopic image showing the details of the rigid polymer reinforced hydrogel cube. (Photo Credit: Honggeng Li, Singapore University of Technology and Design and Hunan University)

Note S2: Fig. S2 present the possible chemical structures at the interface between Acrylamide-PEGDA hydrogel and (meth)acrylate polymer (Fig. S2A). It should be noted that because

PEGDA/acrylamide mixing ratio (0.625-1.25 wt. %) is low in the high water content (70-80 wt.%) AP hydrogel system, the majority of the hydrogel-polymer interfacial bonds are formed by connecting the acrylamide in hydrogel with the (meth)acylate functional group in polymer as presented in Fig. S2B; but there might be a small number of the hydrogel-polymer interfacial bonds between PEGDA and (meth)acylate polymer as presented in Fig. S2C.

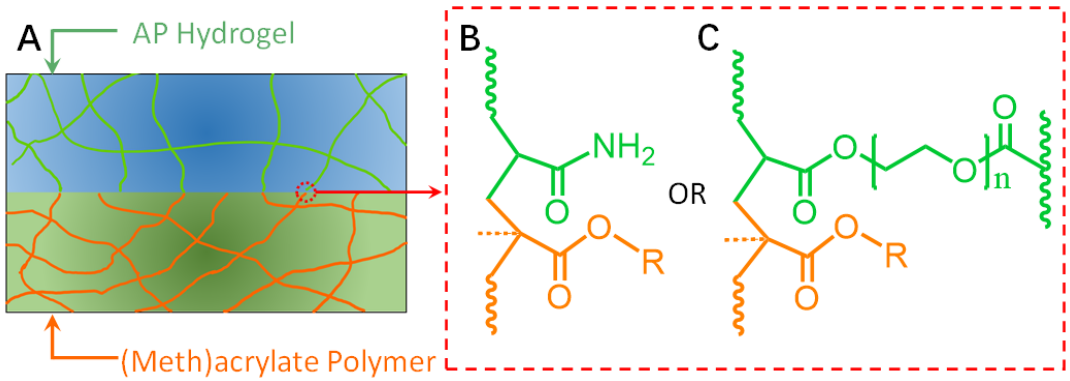

Fig. S2. Chemical structures at the hydrogel-polymer interface. (**A**) Schematic of the AP hydrogel-(meth)acrylate polymer interface. (**B**) Covalent bonds between acrylamide functional group in hydrogel and (meth)acrylate functional group. (**C**) A small number of covalent bonds between acrylate functional group of PEGDA in hydrogel and (meth)acrylate functional group in polymer.

Note S3: To compare the photopolymerization kinetics of the hydrogels initiated by TPO and I2959 (Fig. 3B), we prepared the hydrogel samples by using the FTIR protocol described in Materials and Methods, but UV curing the aqueous solutions with a fix thickness of 140 μm under the near UV light (405 nm) for given time intervals from 5 seconds to 2 minutes. For each sample, infrared spectra were recorded in the range 4000-400 cm^{-1}. The conversion of acrylamide was calculated from the decay/disappearance of the peak at 988 cm^{-1}, which is the out-of-plane bending mode of the $-CH_2-$ unit (methylene group), normalized to the C=O stretching peak (carbonyl group) at 1655 cm^{-1} as an internal standard. Fig. S3 shows the decay

peaks of the methylene group after normalization for the hydrogel solutions with TPO nanoparticles and I2959 as photoinitiator, respectively.

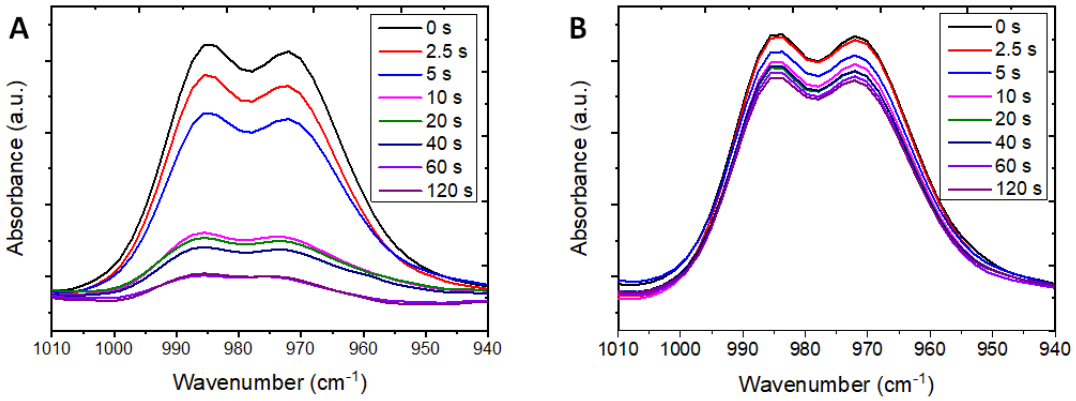

Fig. S3. FTIR characterizations to investigate the photopolymerization kinetics. (A) The AP hydrogel initiated by the water-soluble TPO. (B) The AP hydrogel initiated by Irgacure 2959.

Note S4: Uniaxial tensile tests of pure hydrogels, pure UV curable polymers, and hydrogel-polymer hybrid samples were conducted on an MTS uniaxial testing machine (Criterion Model 43, MN USA). The strain rate was 5 mm/min. The results are presented in Fig. S4.

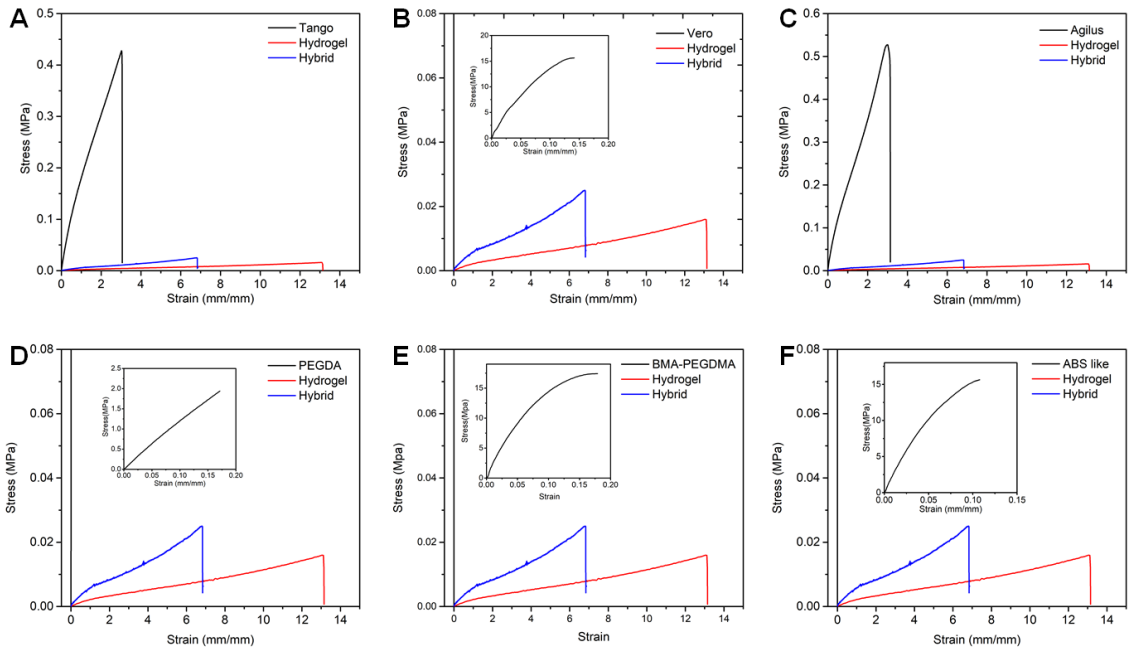

Fig. S4. The stress-strain curves of a pure hydrogel sample, a pure 3D printed polymer, and a hydrogel-polymer hybrid. (**A**) Hydrogel with Tango elastomer. (**B**) Hydrogel with Vero rigid polymer. (**C**) Hydrogel with Agilus elastomer. (**D**) Hydrogel with PEGDA. (**E**) Hydrogel with BMA-PEGDMA SMP. (**F**) Hydrogel with ABS-like rigid material.

Note S5: We performed the peeling tests to investigate the interfacial bonding between hydrogel and two different polymers (*12*). Fig. S5A presents the illustration of the 180°-peeling tests where the UV curable polymer is bonded to a rigid polymeric substrate; a polymeric backing layer is attached to the hydrogel to constrain its deformation; and the hydrogel and the UV curable polymer are bonded in an area of 20 mm × 20 mm. All the materials are chemically bonded, and the thickness of hydrogel and polymer layer is 4 mm. The peeling tests were conducted on an MTS uniaxial testing machine (Criterion Model 43, MN USA). The strain rate was 10 mm/min. Fig. S5B show the process of the peeling tests to investigate the interfacial bonding between hydrogel and UV curable polymer. The processes of the peeling tests also can be found in Movie S4. As shown in Fig. S5C, the measured interfacial toughness for the AP hydrogel on the six different UV curable polymers are similar to each other. This similarity can be explained by the fracture images of the hydrogel-polymer samples during the peeling tests (Fig. S5D). It can be seen that the AP hydrogel, instead of the hydrogel-polymer interface, undergoes a cohesive failure near the interface during the peeling tests, which leaves a residual layer of hydrogel on the polymer substrates (Fig. S5D). The peeling tests confirm that the energy needed to break the hydrogel-polymer interface is greater the energy needed to break the hydrogel itself.

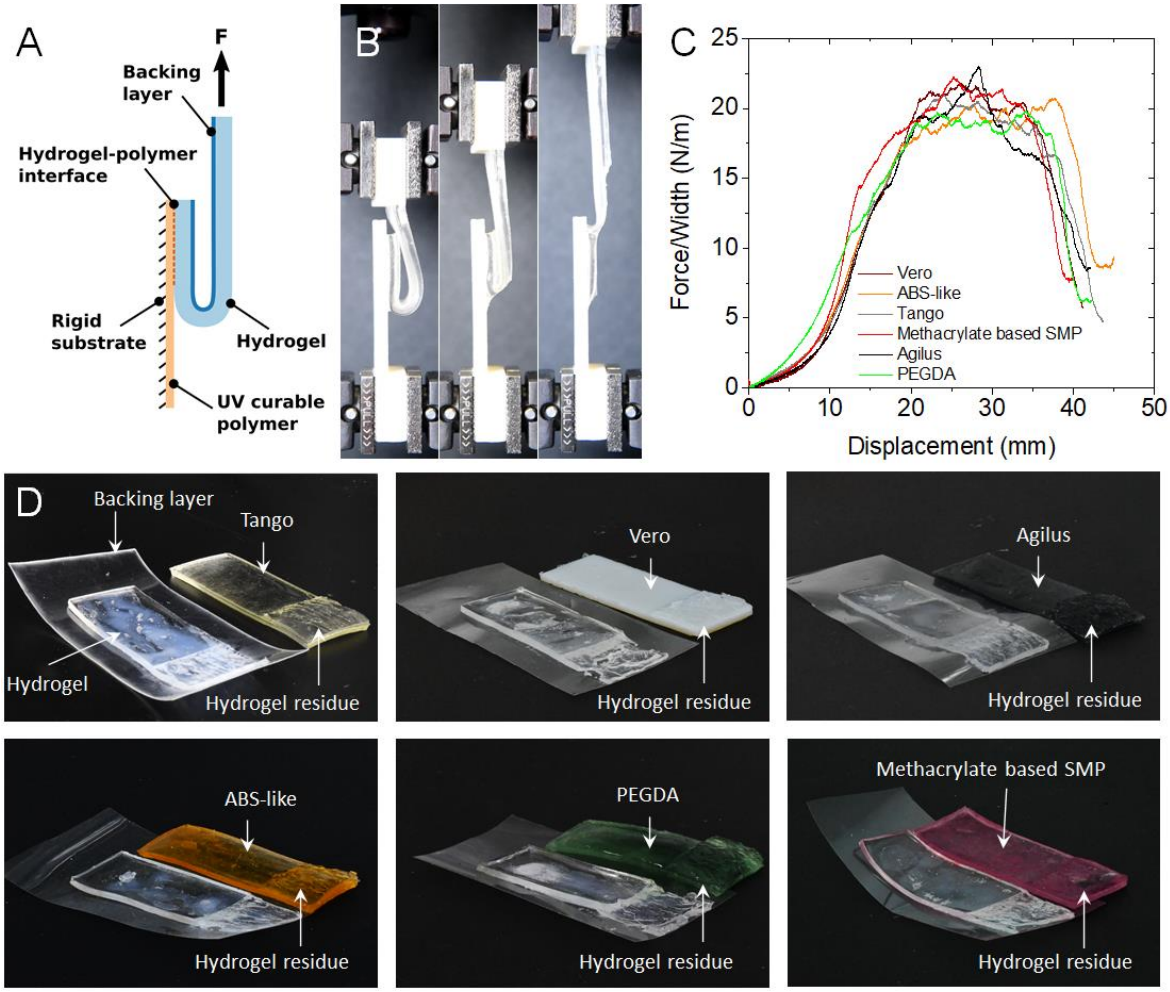

Fig. S5. Peeling test to investigate hydrogel-polymer interfaces. (**A**) Illustration of 180°-peeling test. (**B**) Peeling test to investigate the interfacial bonding between hydrogel and polymer, respectively. (**c**) The force/width-displacement curves to investigate the interfacial toughness. (**D**) Snapshots of ruptured hydrogel-polymer samples. (Photo Credit: Zhe Chen, Zhejiang University)

Note S6: we perform the peeling tests on the AP hydrogel-Tango elastomer hybrid samples where the AP hydrogels are cured with different time to investigate the effect of UV curing time on the interfacial toughness. Fig. S6A present the relation between interfacial toughness and curing time. Fig. S6B shows the force/width-displacement curves during the peeling tests. The measured peeling force reaches a plateau (with slight oscillation), as the peeling process entered steady state. The interfacial toughness Γ is determined by dividing the plateau force F by the width of the hydrogel sheet W. In the peeling tests, the dimensions of each hydrogel and Tango part are 50 mm × 20 mm × 1 mm (Length × Width × Thickness), and the overlapping

area between the AP hydrogel and Tango is 20 mm × 15mm (Length × Width). Fig. S6C presents the relation the toughness of pure hydrogel and curing time. The experiments follow the protocol reported in previous work *(29)*. Fig. S6D shows the interface image during the peeling test where the hydrogel undergoes the cohesive failure that leaves the hydrogel residue on the Tango elastomer. Fig. S6E-I present the images of the fractured hydrogel-Tango hybrid samples where the AP hydrogels are cured with different times. All the hydrogel-elastomer hybrid samples facture on the hydrogel side, and all fractures are cohesive even for the hybrid sample where the hydrogel is only cured with 10 s.

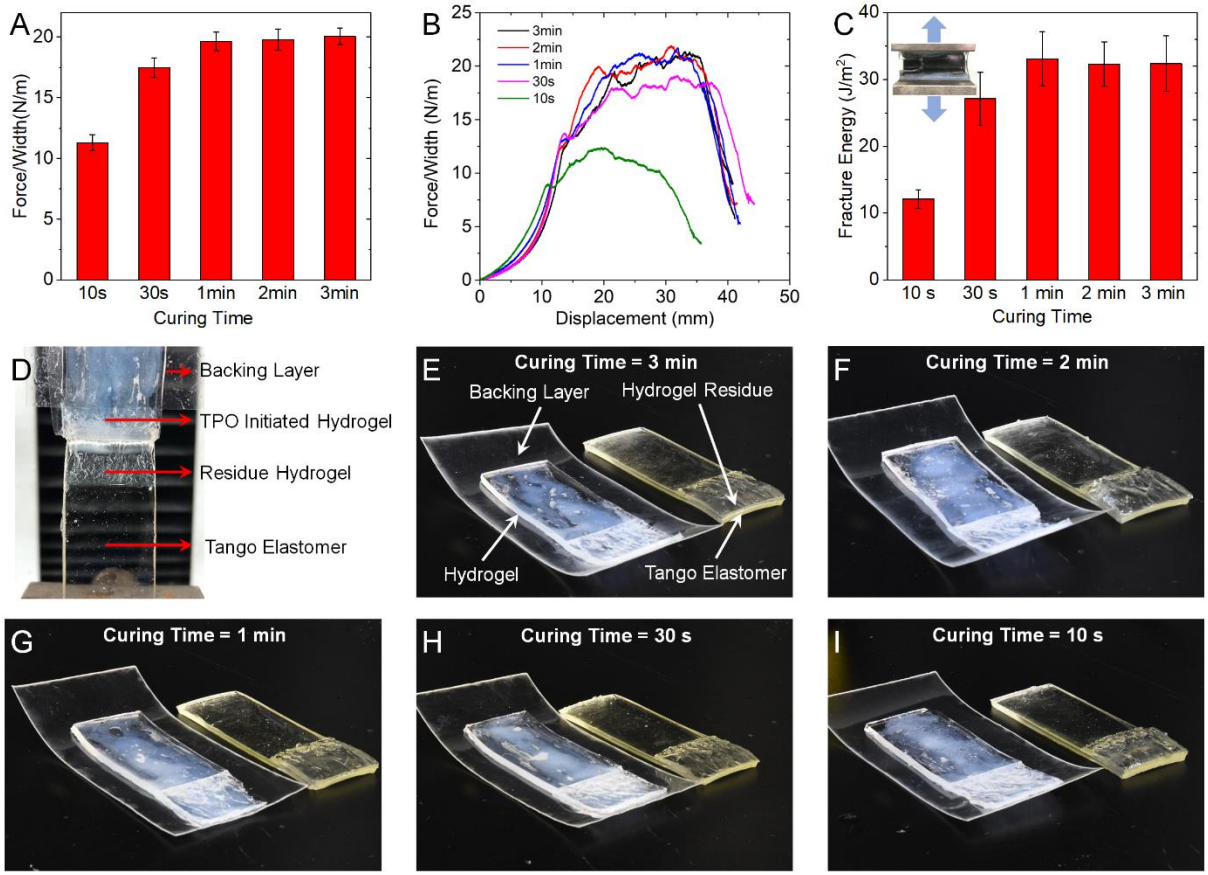

Fig. S6. Peeling tests to investigate the effect of curing time on the interfacial toughness and fracture mode. (**A**) Measured interfacial toughness of the AP hydrogel-Tango elastomer hybrid samples where the AP hydrogels are cured with different times. (**B**) The force/width-displacement relation for the peeling tests. (**C**) Fracture energy of pure AP hydrogel samples cured with different times. (**D**) Image of the hydrogel-Tango interface during peeling test. (**E**)-

(**I**) Images of the fractured AP hydrogel-Tango hybrid samples where the AP hydrogels are cured with different times. (Photo Credit: Zhe Chen, Zhejiang University)

Note S7: we perform the peeling test to investigate the interfacial bonding between the Tango elastomer and AP hydrogel with photoinitiator-I2959 which is cured in an oxygen free environment under 254 nm wavelength UV curing for 40 min. Figure S7 shows that the I2959 initiated AP hydrogel undergoes cohesive failure indicating that proposed interfacial bonding mechanism also works for the I2959 initiated AP hydrogel which could be used to print AP hydrogel with other polymers through DIW based 3D printing.

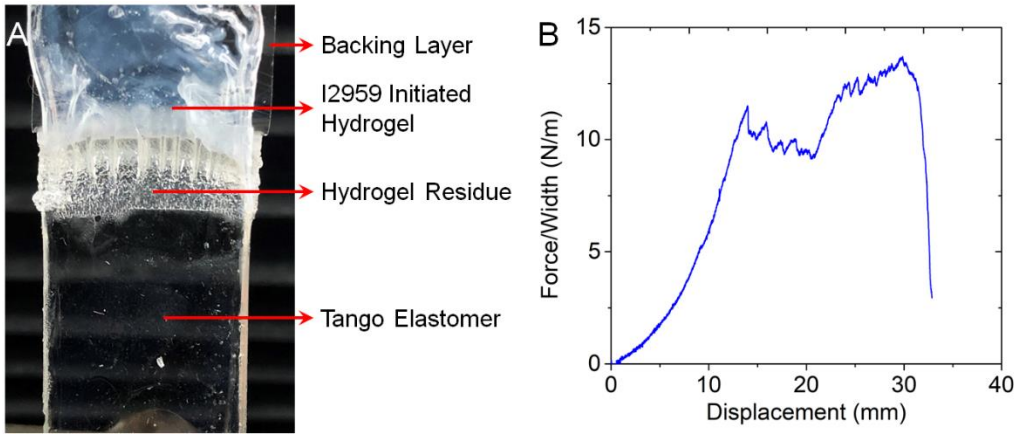

Fig. S7. Peeling test for the AP hydrogel-Tango elastomer hybrid sample where the AP hydrogel is initiated by water-soluble photoinitiator-I2959. (**A**) The image of the I2959 initiated hydrogel-Tango interface during peeling test. (**B**) The force/width-displacement relation for the peeling tests. (Photo Credit: Zhe Chen, Zhejiang University)

Note S8: We characterized the compressive stress-strain behavior of rigid polymer reinforced hydrogel by first printing the reinforced cubes with different rod diameters (Fig. S8A), and pressing them on a MTS uniaxial testing machine (Criterion Model 43, MN USA) with the strain rate of 5 mm/min. Supplementary Fig. S8B plots the compressive stress-strain behaviour of reinforced hydrogel cubes with different rods compared with pure hydrogel.

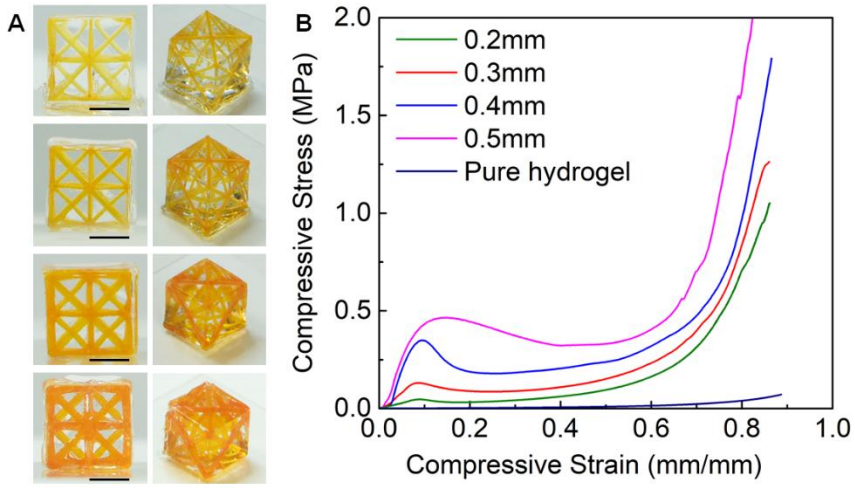

Fig. S8. The compressive stress-strain behaviour of rigid polymer reinforced hydrogel cubes. (**A**) Snapshots of the printed reinforced hydrogel cubes (scale bar: 5 mm). (**B**) The compressive stress-strain behaviour of reinforced hydrogel cubes with different rods compared with pure hydrogel. (Photo Credit: Zhe Chen, Zhejiang University)

Note S9: we performed shape memory cycling test on a dynamic mechanical analyzer (DMA, TA Q800) to characterize the shape memory behavior of the modified Vero based SMP. As shown in Fig. S9, we first stretched Vero sample at 37 °C by 44% (ε_p = 44%), then decrease the temperature from 37 °C to 20 °C at a cooling rate of 2 °C/min while keeping the deformation at 44%. After the temperature arrived at 20 °C, the temperature was kept at 20 °C for 2 min. Then, the external loaded was suddenly removed, and the fixed strain was measured as 43% (ε_u = 43%). Therefore, we can calculate the shape fixing ratio (R_f) following the equation $R_f = \varepsilon_u / \varepsilon_p$, and R_f = 97.7%. The shape recovery process was initiated by heating the SMP sample from 20 °C back to 37 °C at a heating rate of 2 °C/min. During this process, the shape recovery strain $\varepsilon(t)$ varies over time, and the shape recovery ratio R_r can be calculated as $R_r = (\varepsilon_u - \varepsilon_r)/\varepsilon_u$. After the heating started for 60 min, $\varepsilon(t)$ is reduced to 0.7%, and the shape recovery ratio R_r is 98.4%.

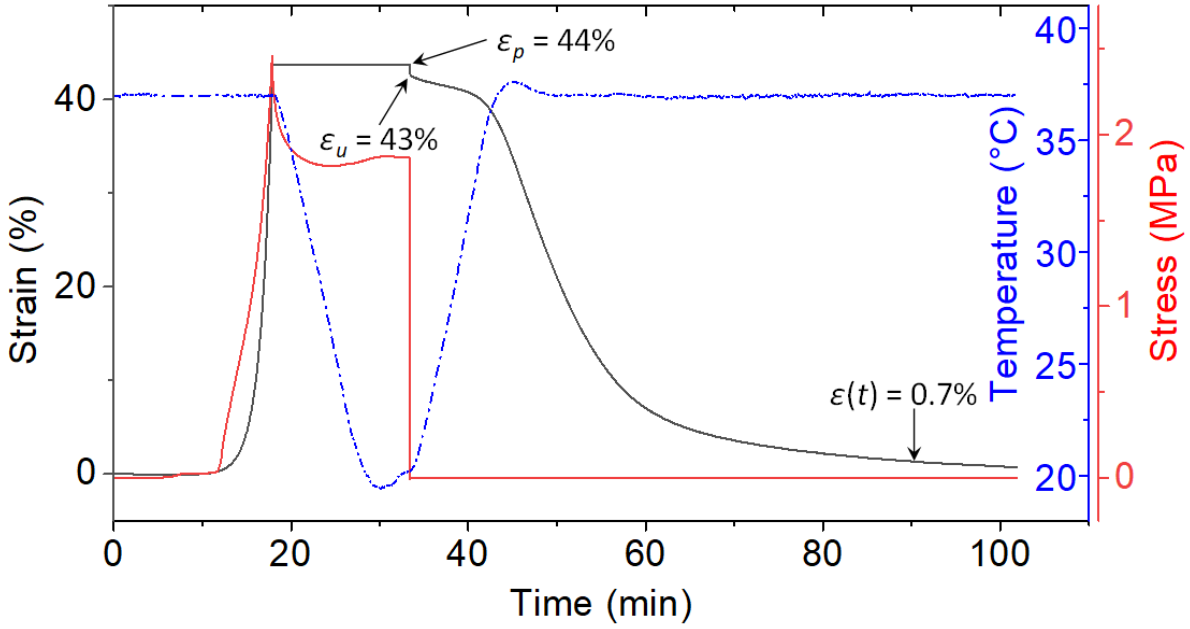

Fig. S9. Shape memory cyclic test of the modified Vero SMP sample.

Note S10: we quantified the drug releasing process by measuring Ultraviolet-Visible light absorbance of the PBS buffer samples taken from the PBS solution where the SMP-hydrogel stent was immersed for different durations. We loaded red dye as “drugs” to the hydrogels of the stent. The SMP-hydrogel stents were placed in a 250 mL breaker which contained 100 mL of PBS buffer (pH: 7.4, temperature: 37 °C). The red dye particles gradually diffuse into the PBS solution. We took out 3 mL samples from the breaker at each predetermined time point. The absorbance of each sample was measured on a Spectrometer (PerkinElmer Lamda 950 UV/Vis/NIR Spectrometer). The wavelength range of the light spectrum is 400 nm~700 nm. As presented in Fig. S10A, the sample taken from the PBS solution which the stent was placed for longer duration has higher the absorbance. In order to build the relation between light absorbance and the release amount of the red dye, we first measured absorbance of the PBS buffer solutions added with different red dye concentrations (Fig. S10B). The results show that the maximum absorption wavelength of the red dye is 554 nm. In Fig. S10C, we can achieve

the standard curve equation by linear regression of concentration (C) to absorbance intensity at 554 nm ($I_{554\,nm}$) as follows:

$$I_{554nm} = 0.026C - 0.001. \qquad \text{(Eq. S1)}$$

Then, we can calculate the release amount of red dye from the SMP-hydrogel stent at each time points according to the standard curve in Eq. S1. The cumulative release percentage of the red dye Q can be further calculated by the following equation:

$$Q = \frac{m_0 + m_1}{m} = \frac{(C_1 + C_2 + \cdots + C_n)V_0 + C_n \cdot V_1}{n}, \qquad \text{(Eq. S2)}$$

where m is the total mass of red dye in the stent, m_0 is the mass of red dye taken out from the breaker at each predetermined time point, m_1 is the mass of dye in breaker, n is the total amount of dye, V_0 is 3 mL, V_1 is 100 mL, C_n is the concentration at each predetermined time point.

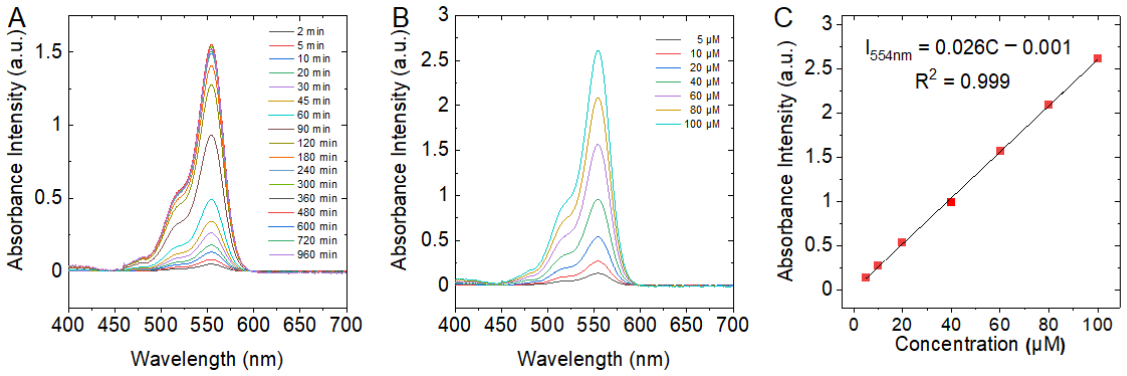

Fig. S10. UV-Vis spectra to quantify the drug release process. (**A**) UV-Vis spectra of the PBS samples where the stent was immersed for different durations. (**B**) UV-Vis spectra of the PBS solution loaded with given concentration of red dyes. (**C**) The standard curve achieved from **B**.

Note S11: after being placed in the Phosphate Buffered Saline (PBS) buffer solution for 24 hours, the SMP-hydrogel stent released all the red dyes, and the hydrogel skins became swollen and transparent (Fig. S11A). In Fig. S11B, the SMP rod surrounded by the hydrogel skin can be clearly seen through the transparent hydrogel skin.

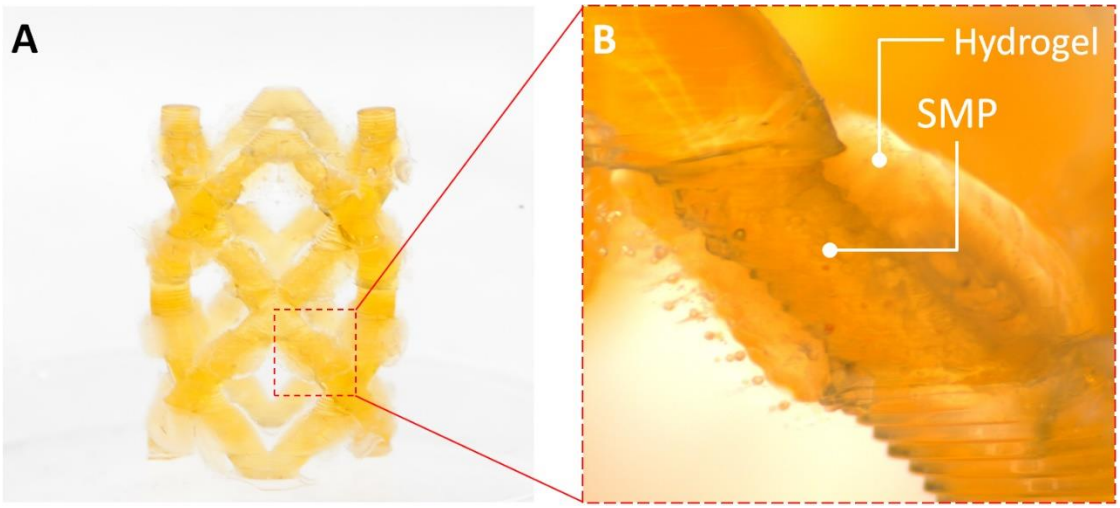

Fig. S11. Snapshots of the SMP-hydrogel stent which has been immersed in the PBS solution for 24 hours. (A) Entire stent. (B) Zoom-in image of the stent rod. (Photo Credit: Jianxiang Cheng, Southern University of Science and Technology)

Note S12: Fig. S12A-D present a 3D printed lattice cube which is not only conductive, but also highly deformable. More importantly, the strong bonding between hydrogel and elastomer allows us to print the multimaterial lattice structure which has a conductive hydrogel core protected by the elastomer skin (Fig. S12E) to prevent dehydration which is a critical challenge for the hydrogel based devices and machines. We carry out dehydration comparison tests to exam the effect of the elastomer skin on the anti-dehydration. The ionic conductive hydrogel contains 70 wt.% of water and about 5.6% of lithium chloride. The conditions of dehydration testing are 27 °C and 80% humidity. Through the comparison (Fig. S12F), we find that the lattice structure protected by the elastomer skin does not exhibit noticeable change in its weight over 48 h, while the unprotected hydrogel structure loses 40 % water after 48 h, demonstrating the effective anti-dehydration of the elastomer protective skin.

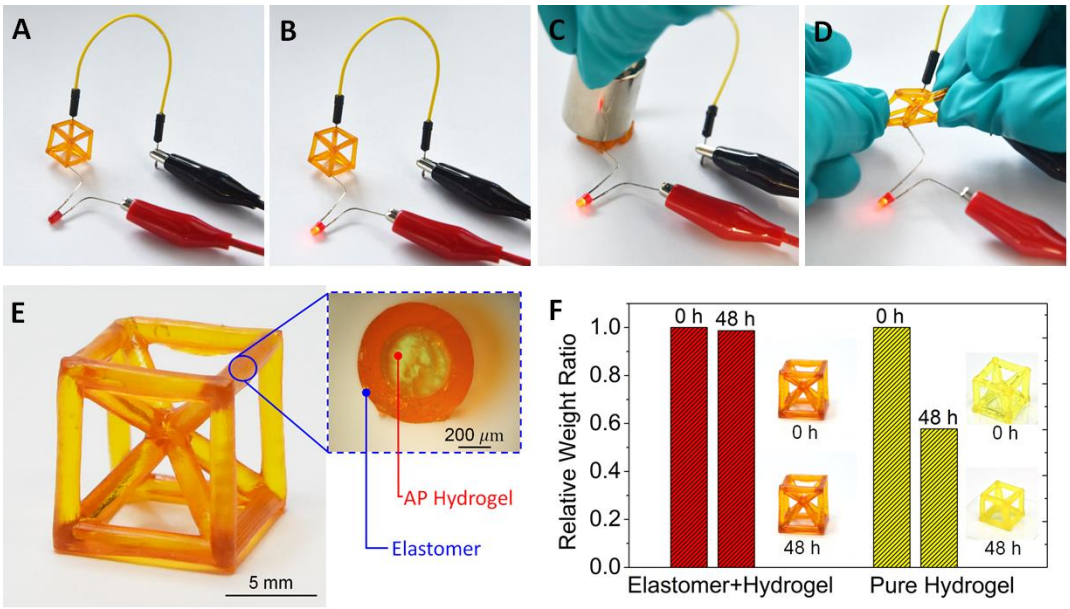

Fig. S12. 3D printed conductive hydrogel lattice structure with elastomer protective skin. (**A**-**D**) Demonstrations of conductivity and deformability of the lattice structure. (**A**) Power off; (**B**) power on; (**C**) being pressed; (**D**) being stretched. (**E**) Details of the printed hydrogel lattice structure. (**F**) Comparison of anti-hydration tests. (Photo Credit: Zhe Chen, Zhejiang University)

Note S13: Fig. S13 presents the layout of the ionic hydrogel strain sensor. In general, the strain sensor is constructed by connecting N long segments (red color, $N = 4$) and N-1 short segments (blue color). The long segment has length L_1, width L_2 and thickness L_3. The short segment has length l_1, width l_2 and thickness l_3 (note $L_2 = l_2$, $L_3 = l_3$). When the strain sensor is at the initial undeformed state, the cross-section area of the long segment A_0 equals to L_2L_3, and the cross-section area of the short segment A_0' is l_2l_3. The resistance of the strain sensor R_0 is

$$R_0 = N \cdot \left(\rho \frac{L_1}{A_0} \right) + (N\text{-}1) \cdot \left(\rho \frac{l_1}{A_0'} \right) = a + b \,. \qquad \text{(Eq. S1)}$$

Here, ρ is the resistivity of the ionic conductive hydrogel; a and b are constants. Once a stretch λ is applied along the x direction, the length of the long segment becomes λL_1, and the width of the short segment becomes λl_2. Since the strain sensor is incompressible, we have

$\lambda\lambda_y\lambda_z = 1$. Therefore, $\lambda_y = \lambda_z = \lambda^{-1/2}$. Base on this, the width and thickness of the long segment are $\lambda^{-1/2}L_2$ and $\lambda^{-1/2}L_3$ respectively; the length and thickness of the short segment are $\lambda^{-1/2}l_1$ and $\lambda^{-1/2}l_3$. We can further calculate the current cross-section areas for long the short segments: $A = \lambda^{-1}L_2L_3 = \lambda^{-1}A_0$ and $A' = \lambda^{1/2}l_2l_3 = \lambda^{1/2}A_0'$. Thus, when the sensor is under stretch λ, the resistance of the strain sensor $R(\lambda)$ is

$$R(\lambda) = N \cdot \left(\rho \frac{\lambda L_1}{\lambda^{-1}A_0}\right) + (N\text{-}1) \cdot \left(\rho \frac{\lambda^{-1/2}l_1}{\lambda^{1/2}A_0'}\right) = a\lambda^2 + b\lambda^{-1}. \quad \text{(Eq. S2)}$$

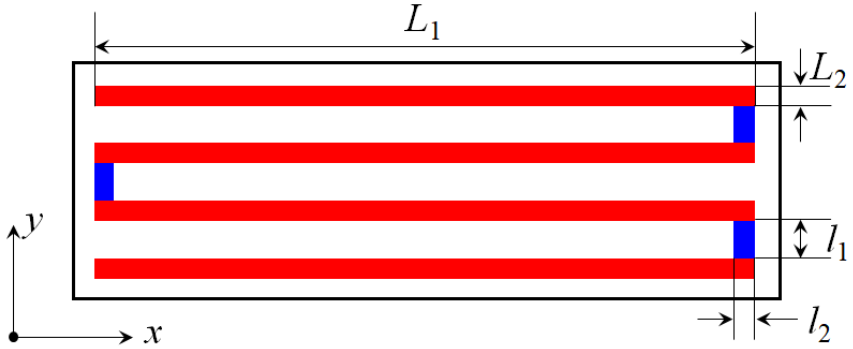

Fig. S13. The layout of the ionic hydrogel strain sensor.

Note S14: Table S1 and S2 summarize the literature reviews that compare the demonstrations in Fig. 4 and Fig. 6 from this work with the counterparts reported in previous papers in terms of fabrication process, mechanical performance and functionality.

Table S1. Comparison on 3D printed hydrogel composites reported from different papers.

		This Work	Ref. [33]	Ref. [34]	Ref. [35]	Ref. [13]
Constituent	Hydrogel	PAAm-PEGDA	PAAm	PAAm-Alginate	GelMA	PAAm-Alginate
	Fiber	Vero	Emax	Emax	PCL	PLA
Hydrogel	Modulus (E_H)	7 kPa	260 kPa	350 kPa	12 kPa	70 kPa
	Elongation at Break	1200%	70%	38%	50%	1900%

Composite	Modulus (E_C)	**0.2-5 MPa**	0.77-2.3 MPa	0.54-2.1 MPa	100-400 kPa	0.66-6.37 MPa
	Failure strain	**80-180%**	74-170%	42-67%	150%	280-380%
	Reinforcing ratio (E_C/E_H)	**29-714**	3-9	1.5-6	8-33	9.5-91
Fabrication Method	3D Printing Technology	DLP	DIW	DIW	Hydrogel: Molding Fiber: EHD	Hydrogel: Molding Fiber: FDM
	Dimensions of Structure	**3D**	2.5D	2.5D	2D	2D

* Polyacrylamide - PAAm; Poly(ethylene glycol) diacrylate - PEGDA; Gelatin methacrylamide -GelMA; Polycaprolactone - PCL; Polylactide - PLA; Digital Light Processing - DLP; Direct Ink Writing - DIW; Electro Hydrodynamic - EHD; Fused Deposition Modeling - FDM.

Table S2. Comparison on pneumatic soft actuators reported from different papers.

	Fabrication Process	Material of Sensor	Sensed Bending
This work	1. Entire actuator was fabricated in **one** DLP based multimaterial **fabrication process**.	Ionic conductive PAAm-PEGDA hydrogel	From **-30°** to 120°.
Ref. [45]	1. Using dual-material FDM printer to fabricate the strain sensing layer; 2. Using FDM printer to fabricate the actuator body; 3. Welding the strain sensing layer with the actuator body.	Conductive PLA	From 0° to 25°
Ref. [46]	1. Actuator body: molding and 3 hours thermal curing at 65 °C; 2. Strain limiting PDMS layer: molding and 3 hours thermal curing at 65 °C; 3. Salination of PDMS surface: 3 hours thermal curing at 65 °C; 4. Hydrogel sensor layer: 3 hours thermal curing at 65 °C.	Ionic conductive PAAm-MBAA hydrogel	From 0° to **160°**.
Ref. [47]	1. Fabricating actuator mold; 2. Molding and thermal curing silicon rubber actuator body; 3. Fabricating conductor mesh mold; 4. Molding the electronic conductive sensing layer; 5. Integrating the actuator body with the sensing layer.	Silver ink	From 0° to ~120°
Ref. [48]	1. 3D printing actuator body mold; 2. Molding and thermal curing silicone rubber actuator body; 3. Masking and brushing the CNT strain sensor; 4. Masking and brushing the AgNW conductive circuit; 5. Encapsulate the strain sensor with PDMS; 6. Embedding the strain sensor to the	CNT for strain sensor; AgNW for conductive circuit.	From 0° to ~90°

	actuator.		

* Polydimethylsiloxane – PDMS; N,N'-methylenebis (acrylamide) – MBAA; Carbon nanotube – CNT; Silver Nanowire – AgNW.

Note 13: Table S3-S7 present the estimated printing time of structures shown in Fig. 1D, Fig. 1F, Fig. 4A, Fig.4D, Fig. 4G, Fig. 5A, and Fig. 6A, respectively.

Table S3. Diagonally symmetric Kelvin form in Fig. 1D.

Height		0-10 mm
Layer Number (140 μm/layer)		72
AP Hydrogel with Sudan I	Curing time	20 s × 72
	Time of Vertical stage motion	1.5 s × 72
	Time of horizontal stage motion and air jetting	1.5 s × 72
TangoPlus	Curing time	3 s × 72
	Time of Vertical stage motion	1.5 s × 72
	Time of horizontal stage motion and air jetting	1.5 s × 72
Estimated total fabrication time		2088 s (34.8 min)

Table S4. Kelvin form consisting of three materials arranged in series in Fig. 1F.

Height		0-3.333 mm	3.333-6.666 mm	6.666-9.999 mm
Layer Number (140 μm/layer)		24	24	24
TangoPlus + Sudan I	Curing time	5 s × 24		
	Time of Vertical stage motion	1.5 s × 24		
	Time of horizontal stage motion and air jetting	1.5 s × 1		
AP Hydrogel + Quinoline Yellow	Curing time		20 s × 24	
	Time of Vertical stage motion		1.5 s × 24	
	Time of horizontal stage motion and air jetting		1.5 s × 1	
VeroBlack	Curing time			5 s × 24
	Time of Vertical stage motion			1.5 s × 24
	Time of horizontal stage motion and air jetting			1.5 s × 0
Estimated total fabrication time			831 s (13.85 min)	

Table S5. Horseshoe structure reinforced hydrogel composite mat in Fig. 4A.

Height		0-1 mm
Layer Number (140 μm/layer)		8
AP Hydrogel	Curing time	15 s × 8
	Time of Vertical stage motion	1.5 s × 8
	Time of horizontal stage motion and air jetting	1.5 s × 8
VeroBlack	Curing time	5 s × 8
	Time of Vertical stage motion	1.5 s × 8
	Time of horizontal stage motion and air jetting	1.5 s × 8
Estimated total fabrication time		208 s (3.5 min)

Table S6. Lattice structure reinforced hydrogel composite cube in Fig. 4D.

Height	0-10 mm

Layer Number (140 μm/layer)		72
AP Hydrogel	Curing time	15 s × 72
	Time of Vertical stage motion	1.5 s × 72
	Time of horizontal stage motion and air jetting	1.5 s × 72
VeroClear + Sudan I	Curing time	5 s × 72
	Time of Vertical stage motion	1.5 s × 72
	Time of horizontal stage motion and air jetting	1.5 s × 72
Estimated total fabrication time		1872 s (31.2 min)

Table S7. Lattice structure reinforced hydrogel meniscus structure in Fig. 4G.

Height		0-4.7 mm
Layer Number (140 μm/layer)		34
AP Hydrogel	Curing time	15 s × 34
	Time of Vertical stage motion	1.5 s × 34
	Time of horizontal stage motion and air jetting	1.5 s × 34
VeroClear + Sudan I	Curing time	5 s × 34
	Time of Vertical stage motion	1.5 s × 34
	Time of horizontal stage motion and air jetting	1.5 s × 34
Estimated total fabrication time		884 s (14.7 min)

Table S8. Shape memory stent with hydrogel core in Fig. 5F.

Height		Pure SMP: 9 mm	SMP + Hydrogel: 5.5 mm
Layer Number (140 μm/layer)		65	39
Modified VeroClear + Sudan I	Curing time	10 s × 65	5 s × 39
	Time of Vertical stage motion	1.5 s × 65	1.5 s × 39
	Time of horizontal stage motion and air jetting	1.5 s × 1	1.5 s × 39
AP Hydrogel + Red Dye	Curing time		30 s × 39
	Time of Vertical stage motion		1.5 s × 39
	Time of horizontal stage motion and air jetting		1.5 s × 39
Estimated total fabrication time			2348 s (39.1 min)

Table S9. Pneumatic soft actuator with hydrogel strain sensor in Fig. 6A.

Height		0-0.5 mm	0.5-1.5 mm	1.5-13 mm
Layer Number (140 μm/layer)		4	7	82
TangoPlus	Curing time	3 s × 4	3 s × 7	
	Time of Vertical stage motion	1.5 s × 4	1.5 s × 7	
	Time of horizontal stage motion and air jetting	1.5 s × 1	1.5 s × 7	
AP Hydrogel + Rhodamine	Curing time		20 s × 7	
	Time of Vertical stage motion		1.5 s × 7	
	Time of horizontal stage motion and air jetting		1.5 s × 7	
TangoPlus	Curing time			3 s × 82
	Time of Vertical stage motion			1.5 s × 82
	Time of horizontal stage motion and air jetting			1.5 s × 0
Estimated total fabrication time			591.5 s (9.86 min)	